

## Article

# Bayesian analysis of hybrid neutron star EoS constraints within an instantaneous nonlocal chiral quark matter model

Alexander Ayriyan<sup>1,2</sup> , David Blaschke<sup>1,3,4</sup> , Juan Pablo Carlomagno<sup>5,6</sup> , Gustavo A. Contrera<sup>5,6</sup>  and Ana Gabriela Grunfeld<sup>5,7</sup> \*

<sup>1</sup> Institute for Theoretical Physics, University of Wrocław, Max Born Pl. 9, 50-204, Wrocław, Poland

<sup>2</sup> A. Alikhanyan National Science Lab, Alikhanyan Brothers street 2, 0036 Yerevan, Armenia

<sup>3</sup> Helmholtz-Zentrum Dresden-Rossendorf (HZDR), Bautzner Landstrasse 400, 01328 Dresden, Germany

<sup>4</sup> Center for Advanced Systems Understanding (CASUS), Untermarkt 20, 02826 Görlitz, Germany

<sup>5</sup> CONICET, Godoy Cruz 2290, Buenos Aires, Argentina

<sup>6</sup> IFLP, UNLP, CONICET, Facultad de Ciencias Exactas, Diagonal 113 entre 63 y 64, La Plata 1900, Argentina

<sup>7</sup> Departamento de Física, Comisión Nacional de Energía Atómica, Av. Libertador 8250, (1429) Buenos Aires, Argentina

\* Correspondence: alexander.ayriyan@uwro.edu.pl

**Abstract:** We present a physics-informed Bayesian analysis of equation of state constraints using observational data for masses, radii and tidal deformability of pulsars and a generic class of hybrid neutron star equation of state with color superconducting quark matter on the basis of a recently developed nonlocal chiral quark model. The nuclear matter phase is described within a relativistic density functional model of the DD2 class and the phase transition is obtained by a Maxwell construction. We find the region in the two-dimensional parameter space spanned by the vector meson coupling and the scalar diquark coupling, where three conditions are fulfilled: 1) the Maxwell construction can be performed, 2) the maximum mass of the hybrid neutron star is not smaller than  $2.0 M_{\odot}$  and 3) the onset density of the phase transition is not below the nuclear saturation density  $n_0 = 0.15 \text{ fm}^{-3}$ . The result of this study shows that the favorable neutron star equation of state has low onset masses for the occurrence of a color superconducting quark matter core between  $0.5 - 0.7 M_{\odot}$  and maximum masses in the range  $2.15 - 2.22 M_{\odot}$ . In the typical mass range of  $1.2 - 2.0 M_{\odot}$ , the radii of these stars are between 11.9 and 12.4 km, almost independent of the mass. In principle, hybrid stars would allow for larger maximum masses than provided by the hadronic reference equation of state.

**Keywords:** Bayesian analysis; hybrid neutron stars; color superconductivity; quark deconfinement

Received:

Revised:

Accepted:

Published:

**Citation:** Ayriyan, A.; Blaschke, D.; Carlomagno, J.P.; Contrera, G.A.; Grunfeld, A.G. Bayesian analysis of hybrid neutron star EOS. *Journal Not Specified* **2025**, *1*, 0. <https://doi.org/>

**Copyright:** © 2025 by the authors.

Submitted to *Journal Not Specified* for possible open access publication under the terms and conditions of the Creative Commons Attribution (CC BY) license (<https://creativecommons.org/licenses/by/4.0/>).

## 1. Introduction

Exploring the phases of matter under extreme conditions, like those in heavy-ion collisions [1] or within neutron stars [2], is a topic that has attracted significant attention over the past decades [3]. We are particularly interested in studying transitions between different phases of strongly interacting matter, like quark-gluon plasma, color superconducting quark matter, and hadronic matter. These transitions have a big impact on astrophysical phenomena like the formation of eccentric binaries and isolated millisecond pulsars (MSPs) [4], binary neutron star mergers [5,6], and even trigger supernova explosions of massive blue supergiant stars [7,8] to mention just a few recent applications.

The status of quark matter as a state of matter in the inner core of neutron stars is still controversial. In particular, since the available data on masses and radii of pulsars do not

allow for a firm model-independent conclusion about a quark deconfinement transition, it has been tried to apply agnostic Bayesian analysis methods to check the evidence for a strong phase transition, see [9] and references therein. In their study, the authors of [9] found evidence against a strong first-order (deconfinement) phase transition in neutron stars. However, since the lightest neutron star to be formed as a result of a supernova explosion according to state-of-the-art simulations has a mass of at least  $1.1 M_{\odot}$ , and there is no scenario available that would explain the existence of a lighter neutron star, the recent measurement of a low mass and radius for HESS J1731-347 [10] has been considered very skeptical in the community. Also because the authors themselves could not present an idea about the origin of a neutron star in the subsolar mass region. Therefore, direct evidence for a strong phase transition from mass and radius measurements in the subsolar mass range is presently lacking the observational basis.

In this situation, we want to suggest a physics-informed Bayesian analysis of modern multi-messenger mass and radius measurements along the lines of our earlier work [11], which can now be made with the new, presently available set of observational data. Such a physics-informed study will be based on a class of hybrid equations of state (EOS) within the two-phase formalism that uses separate models for hadronic and quark matter phases joined by a phase transition construction. Given an appropriate hadronic EOS and the choice of the phase transition construction, there are two free parameters of the color superconducting quark matter model to be determined which cannot be reliably fixed with vacuum properties of hadrons. These are the couplings of the vector meson ( $G_V$ ) and diquark ( $G_D$ ) currents to the corresponding mean fields. As has been shown in [12] using the three-flavor color superconducting Nambu–Jona-Lasinio (NJL) model [13], that with such a setting the required maximum mass  $M_{\text{max}} \sim 2 M_{\odot}$  can be achieved by a sufficiently large  $G_V$ , while an early onset of deconfinement in the range of typical or even subsolar neutron star masses is achieved by a large value of  $G_D$ . In a first systematic study employing this setting, in Ref. [14], the regions in the two-dimensional plane of these two coupling strengths have been identified, where no stable hybrid stars were possible and where the onset of deconfinement is below a certain density. In between these two limits, the lines were shown along which the constraint on the minimal value of the maximum mass could be fulfilled. In these early studies the Dirac-Brueckner-Hartree-Fock (DBHF) hadronic EOS [15] was used together with a Maxwell construction for the phase transition. An alternative study by Baym et al. [16] came to similar conclusions for the preferable region of parameter values in the plane of vector meson and diquark coupling constants using, however, a softer APR-like hadronic EOS and a crossover construction [17], see also the discussion in the review [18]. Studies of quark matter based on the NJL model are limited due to the model's lack of confinement. This feature becomes particularly problematic in applications to the range of finite temperatures, as in supernova explosions and binary neutron star mergers, where it would predict deconfinement at a too low temperature of about 50 – 70 MeV.

In order to overcome this problem, two main routes have been suggested: (A) a confining density functional approach [19] as a relativistic formulation of the string-flip model [20,21] which was recently generalized to include diquark condensation and chiral symmetry [22,23]; and (B) density-dependent quark mass models (see, e.g., [24–31]), in which the bag pressure is interpreted as a density-dependent scalar mean field that can be reinterpreted as a contribution to the dynamical quark mass. The confining models of class (A) can be mapped by a Taylor expansion of the confining density functional w.r.t. the underlying quark bilinears up to second order onto an effective NJL model with medium dependent masses. Equivalently, one can also fit the pressure as a thermodynamic potential of the confining density functional approach by adding a medium dependent bag pressure

and vector meson mean field to the nonlocal NJL model [32,33]. In the present work, we will employ the latter approach to a confining quark matter EOS as the basis for the physics-informed Bayesian analysis to be performed.

## 2. Hybrid neutron star EOS and fitting results

There are two main strategies to construct hybrid neutron star EOS which would fulfill the maximum mass constraint that requires the most massive hybrid star configuration to have at least  $2 M_{\odot}$  at a radius around 12 km. One can start with a nuclear matter EOS that is relatively soft at supranuclear densities, like the well-known variational EOS by Akmal, Pandharipande and Ravenhall (APR) [34] or its updated versions by Togashi and coworkers [35–37]. Then, a crossover construction like the one by Masuda et al. [17] is required to facilitate the transition to a stiffer quark matter EoS at high densities in a thermodynamically consistent way. This strategy has been applied, e.g., by Baym et al. [16] and by Ayriyan et al. [11], who realized the two-zone interpolation scheme (TZIS) that was described in [18]. See also [23] for the extension of the TZIS to finite temperature and multiple critical endpoints.

The alternative is to start from a stiff nuclear EOS, for which a Maxwell construction to a sufficiently stiff quark matter EOS can be performed, so that despite a softening of the EOS due to the phase transition nevertheless the maximum mass constraint can be fulfilled. As examples for such stiff hadronic EOS we mention the DBHF [15] which was used in [12,14] and the relativistic density functional EOS with density-dependent nucleon-meson couplings, denoted as DD2 [38] which was recently used, e.g., in [22,23,33,39–41]. This latter strategy will be applied in the present work.

### 2.1. Nuclear matter phase

For the nuclear matter phase that extends from the core<sup>1</sup> to the crust, we employ the DD2 relativistic density functional EOS with the parametrization described in Ref. [38]. This EOS describes well all known nuclear matter properties including the nuclear symmetry energy and its slope at saturation density  $n_{\text{sat}} = 0.15 \text{ fm}^{-3}$ , as well as the properties of finite nuclei that make their appearance at subnuclear densities defining the crust-core boundary. While in the inner crust these nuclei are still immersed in the Fermi seas of neutrons and electrons (A-e-n phase), the neutron drip density of about  $10^{-4} \text{ fm}^{-3}$  marks the transition to the outer crust made up of nuclei and electrons only (A-e phase).

It is customary to employ a specific EOS for the description of the crust of neutron stars, like the one by Baym, Pethick and Sutherland (BPS) [42], and to match it with the EOS of homogeneous dense nuclear matter phases at the crust-core transition, see Fortin et al. [43]. In the present work, however, we break with this transition by using the EOS table of the generalized RDF (GDRF) which gives a consistent description based on the DD2 interaction of nuclear matter in the density range from  $10^{-9} \text{ fm}^{-3}$  to  $1.0 \text{ fm}^{-3}$ , i.e. from the low-density phases with nuclear clusters to homogeneous nuclear matter, including cluster dissociation. This is described more in detail in the reviews by Oertel et al. [44] and Typel [45]. This GDRF EOS which we call "DD2" throughout this work can be retrieved from the CompOSE repository [46] using the manual [47].

### 2.2. Color superconducting 2SC quark matter

In this work, we consider the scenario of two-flavor color-superconducting quark matter appearing in the cores of NSs at sufficiently high densities. For its description, we

<sup>1</sup> In the case of a hybrid star configuration, this means the outer core being separated by the deconfinement transition from the inner core that is constituted by phases of deconfined quark matter.

employ the 3DFF nonlocal chiral quark model [33] defined by an effective Euclidean action functional that in the case of two light flavors is given by

$$S_E = \int d^4x \left\{ \bar{\psi}(x) (-i\cancel{D} + \hat{m} - \gamma_0 \hat{\mu}) \psi(x) - \frac{G_S}{2} [j_S^f(x) j_S^f(x) + \eta_D [j_D^a(x)]^\dagger j_D^a(x) - \eta_V j_V^\mu(x) j_V^\mu(x)] \right\}. \quad (1)$$

Here  $\hat{m} = \text{diag}(m_u, m_d)$  is the current quark mass matrix with the masses for  $u$  and  $d$  quarks, which are assumed to coincide  $m_u = m_d = 2.3$  MeV, whereas  $\hat{\mu} = \text{diag}(\mu_u, \mu_d)$  is the diagonal matrix for the chemical potentials of  $u$  and  $d$  quarks, which are to be adjusted so as to fulfill charge neutrality and  $\beta$ -equilibrium constraints relevant for neutron star matter. As a result remains the baryon chemical potential  $\mu_B = 3\mu = 3(\mu_u + \mu_d)/2$  as independent thermodynamic variable. The coupling strength in the scalar meson channel is  $G_S = 9.92 \text{ GeV}^{-2}$  and  $\eta_V = G_V/G_S$  ( $\eta_D = G_D/G_S$ ) is the relative coupling in the vector meson (scalar diquark) channel. The currents are given by nonlocal operators based on a separable approximation to the effective one gluon exchange (OGE) model of QCD [48,49],

$$\begin{aligned} j_S^f(x) &= \int d^4z g_S(z) \bar{\psi}(x + \frac{z}{2}) \Gamma_f \psi(x - \frac{z}{2}), \\ j_D^a(x) &= \int d^4z g_D(z) \bar{\psi}_C(x + \frac{z}{2}) i\gamma_5 \tau_2 \lambda_a \psi(x - \frac{z}{2}), \\ j_V^\mu(x) &= \int d^4z g_V(z) \bar{\psi}(x + \frac{z}{2}) i\gamma^\mu \psi(x - \frac{z}{2}), \end{aligned} \quad (2)$$

where we defined  $\psi_C(x) = \gamma_2 \gamma_4 \bar{\psi}^T(x)$  and  $\Gamma_f = (\mathbf{1}, i\gamma_5 \vec{\tau})$ , while  $\vec{\tau}$  and  $\lambda_a$ , with  $a = 2, 5, 7$ , stand for Pauli and Gell-Mann matrices acting on flavor and color spaces, respectively. The functions  $g_i(z)$ ,  $i = S, D, V$ , in Eqs. (2) are nonlocal “instantaneous” form factors (3D-FF) characterizing the effective quark interaction, which depend on the spatial components of the position 4-vector  $z$  only. For the nonlocality a Gaussian ansatz is employed which after Fourier transformation to the momentum space reads

$$g_i(\vec{p}) = \exp(-\vec{p}^2 / \Lambda_i^2), \quad i = S, D, \quad (3)$$

with the 3-momentum vector  $\vec{p}$  and the effective range  $\Lambda_S = \Lambda_D = 885.47$  MeV fitted to Coulomb-gauge lattice QCD data [50]. Note that following [33], in the present work we consider the vector current in Eq. (2) to be local,  $g_V(z) = \delta(z)$ . This restriction could be easily relaxed, see [51]. The equation of state  $p(T, \mu) = T \ln Z(T, \mu)$  for this model follows from the path-integral representation of the partition function  $Z(T, \mu)$  which is evaluated at the mean-field level and results in the pressure  $p_{MF}(\mu_B)$  which, following [33], is augmented by a  $\mu_B$ -dependent bag pressure as in Ref. [32], given by the equation

$$B(\mu_B) = B_0 f_{<}(\mu_B) \quad (4)$$

with

$$f_{<}(\mu_B) = \frac{1}{2} \left[ 1 - \tanh \left( \frac{\mu_B - \mu_{<}}{\Gamma_{<}} \right) \right], \quad (5)$$

where we use  $\mu_{<} = 895$  MeV,  $\Gamma_{<} = 180$  MeV and  $B_0 = 35 \text{ MeV/fm}^3$  as the optimal values to reproduce the astrophysical constraints from multi-messenger astronomy of pulsars. In the present work we are interested in describing the hybrid EOS for cold compact stellar systems. Therefore, we will take the zero-temperature limit. The resulting zero-temperature pressure  $p(\mu_B) = p_{MF}(\mu_B) - B(\mu_B)$  leaves the two couplings  $\eta_V$  and  $\eta_D$  as free parameters of the 3DFF color superconducting quark matter model EOS which forms the basis of the



present work. Each EOS model of the present study can be characterized as a point in the two-dimensional parameter space spanned by the pair  $(\eta_V, \eta_D)$  which will therefore play a central role.

In order to perform a Bayesian Analysis, we fit the above introduced quark matter EoS to the constant speed of sound (CSS) form of the EoS [52]

$$p = A \left( \frac{\mu}{\mu_x} \right)^{1+1/c_s^2} - B \quad (6)$$

where the  $\mu = \mu_B/3$  is the quark chemical potential and  $\mu_x = 1$  GeV sets a scale. Before, such a fit has been provided in [52] for the covariant nonlocal chiral quark model EoS. Here, we present the fit (6) of the 3DFF nonlocal, color superconducting quark matter model [33] in the form

$$A(\eta_D, \eta_V) = a_1 \eta_D^2 + b_1 \eta_V^2 + c_1 \eta_D \eta_V + d_1 \eta_D + e_1 \eta_V + f_1, \quad (7)$$

$$c_s^2(\eta_D, \eta_V) = a_2 \eta_D^2 + b_2 \eta_V^2 + c_2 \eta_D \eta_V + d_2 \eta_D + e_2 \eta_V + f_2, \quad (8)$$

$$B(\eta_D, \eta_V) = a_3 \eta_D^2 + b_3 \eta_V^2 + c_3 \eta_D \eta_V + d_3 \eta_D + e_3 \eta_V + f_3, \quad (9)$$

The fitted parameter values are given in Tab. 1.

**Table 1.** Values of the parameters of Eqs. (7) - (9).

| i | parameter | units                            | $a_i$   | $b_i$   | $c_i$   | $d_i$   | $e_i$   | $f_i$   |
|---|-----------|----------------------------------|---------|---------|---------|---------|---------|---------|
| 1 | $A$       | $\frac{\text{MeV}}{\text{fm}^3}$ | 88.637  | 1.861   | -30.368 | -76.654 | 2.891   | 95.324  |
| 2 | $B$       | $\frac{\text{MeV}}{\text{fm}^3}$ | -192.28 | -10.180 | 30.455  | 390.92  | -28.613 | -100.95 |
| 3 | $c_s^2$   |                                  | 0.142   | -0.071  | 0.066   | -0.166  | 0.134   | 0.427   |

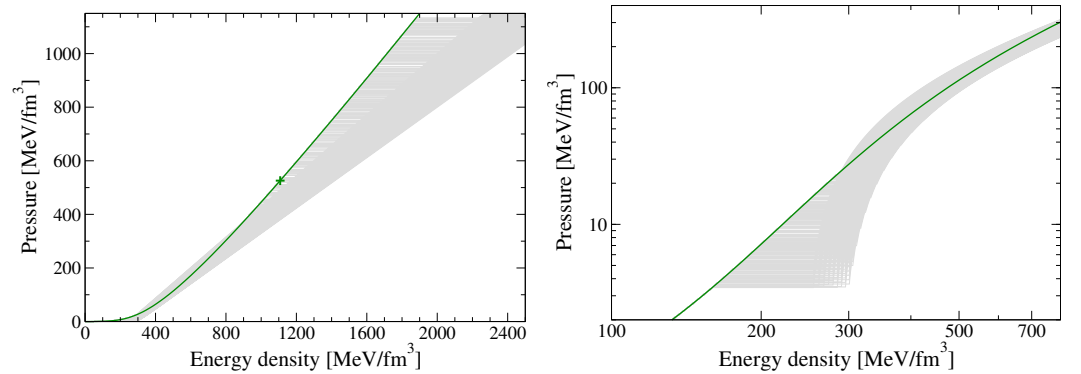


**Figure 1.** Diagram of pressure vs. energy density, which shows the jump in energy density at the phase transition from hadronic DD2 EoS (green solid line) to the color superconducting quark matter EoS in its CSS parametrization (left panel). The right panel shows a closeup of the phase transition region at lower energy densities than that for which the maximum mass configuration of the hadronic DD2 EoS is obtained (indicated by a plus sign on the left panel).

### 2.3. Phase transition construction

We employ the Maxwell construction of the nuclear-to-quark matter phase transition. The resulting EoS is characterized by a critical pressure  $P_c = P_h(\mu_c) = P_q(\mu_c)$  for the onset of the transition from the hadronic phase  $P_h(\mu)$  for  $\mu \leq \mu_c$  to the 2SC quark matter phase  $P_q(\mu)$  for  $\mu \geq \mu_c$  with a jump in energy density  $\Delta\epsilon = \epsilon_q(\mu_c) - \epsilon_h(\mu_c)$ . In Fig. 1, we show

the hybrid neutron star EoS after the Maxwell construction has been performed. In the left panel, we show the whole range of energy densities considered here, while in the right panel a zoom into the region relevant for the phase transition is shown.

For some values of the parameters ( $\eta_D, \eta_V$ ) there is no crossing of the hadronic and quark-matter pressure curves so that no Maxwell construction can be performed. In Fig. 2, we depict the jump in baryon density  $\Delta n = n_q(\mu_c) - n_h(\mu_c)$ , where  $n_i = dP_i(\mu)/d\mu$  for  $i = h, q$  as a contour plot in the  $\eta_D - \eta_V$  plane.

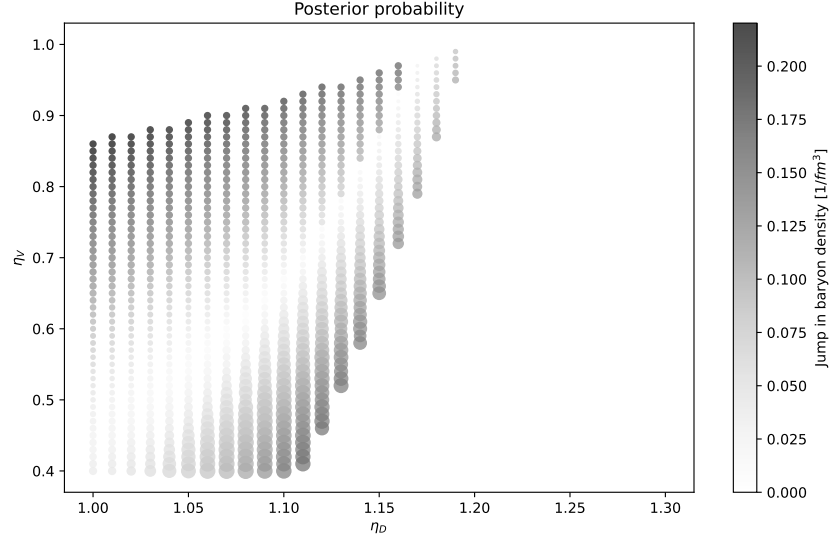


**Figure 2.** Diagram of the coupling constants  $\eta_D - \eta_V$ , which shows jump in baryon density  $\Delta n$  at the phase transition from the hadronic DD2 to the color superconducting 3DFF quark matter EoS. In the parameter region filled with greyscale dots a Maxwell construction is possible. The white spots in the middle of that region stand for parameter sets for which the transition would degenerate to a crossover with  $\Delta n = 0$ .

### 3. Mass, radius and tidal deformability fom TOV solutions

There is a one-to-one relationship between the observable mass-radius relation for neutron stars and the EOS of neutron star matter [53] which follows from the Tolman-Oppenheimer-Volkoff (TOV) equations [54,55] of general relativistic hydrodynamic stability of spherically symmetric, nonrotating compact stars. These equations form the basis for extracting information about the EOS from observations. In the following we will present those mass and radius measurements which provide at present the most promising EOS constraints. In addition, due to the measurement of the gravitational wave signal from the inspiral phase of the binary neutron star merger event GW170817 by the LIGO-Virgo Collaboration [56,57], there is a constraint on the tidal deformability parameter of neutron stars, see [58–60] for the system of differential equations.

In Fig. 3 we show the dependence of the neutron star mass on its central energy density for the EoS parameterizations provided in the previous section. We note that there are cases of hybrid star sequences which have a maximum mass exceeding that of the hadronic DD2 reference EOS shown by the green solid line. On that figure we indicate by a green "X" the location of the maximum mass configuration of the purely hadronic case which has  $M_{\max} = 2.414 M_{\odot}$  and a central energy density  $\epsilon_c^{\max} = 1107.8 \text{ MeV/fm}^3$ .

In Fig. 4 we show as thin black lines the mass-radius relationships that are obtained as solutions of the TOV equations for the set of hybrid EOS introduced in the previous section. For a comparison we show also here as a green solid line the purely hadronic sequence of neutron star configurations that follows for the hadronic baseline EOS DD2. The maximum

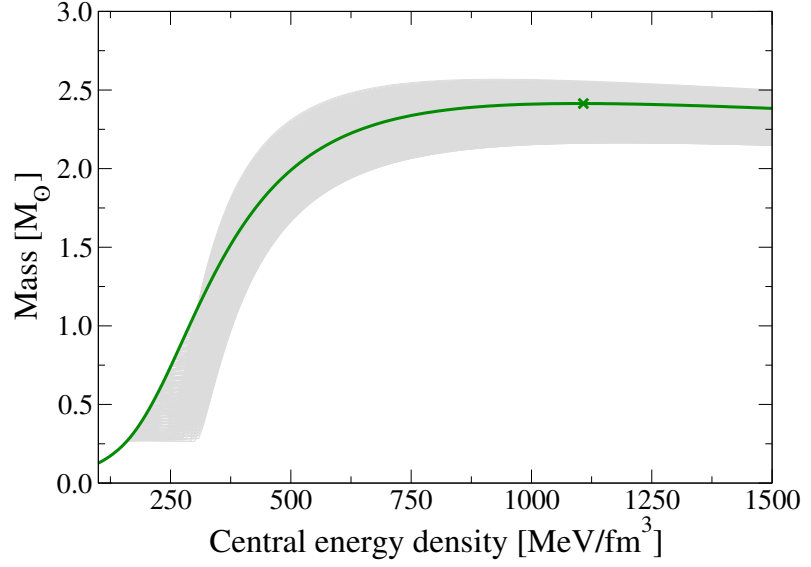


**Figure 3.** Mass versus central energy density for the hybrid EoS with a phase transition from the hadronic DD2 EOS (green line) to color superconducting quark matter described in the nonlocal 3DFF model for varying EOS parameters  $\eta_V$  and  $\eta_D$  (grey lines). The maximum mass configuration among all purely baryonic ones obtained with the DD2 EOS is denoted with a cross on the green line.

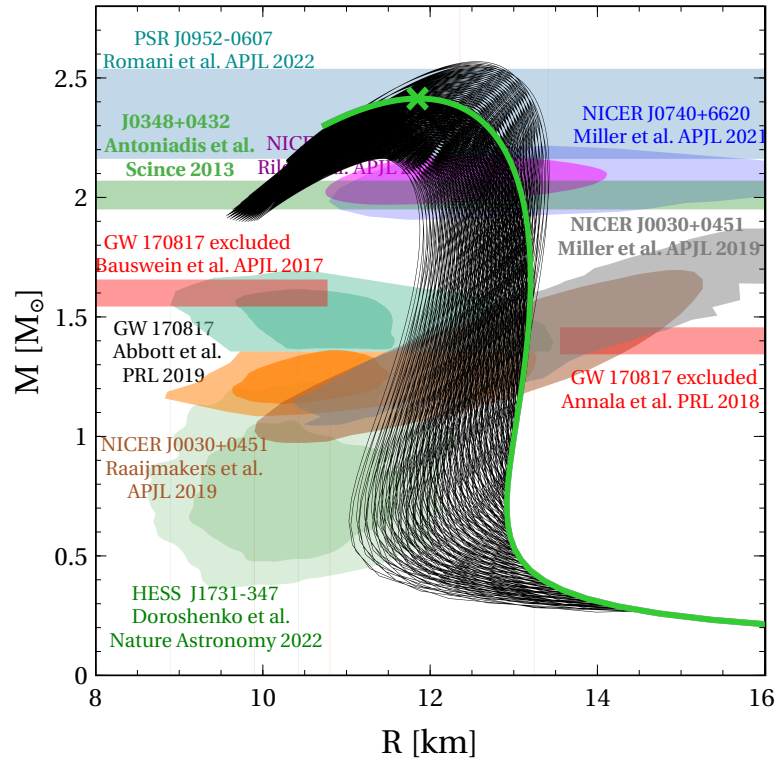


**Figure 4.** Same as Fig. 3 for the mass-radius relations as solutions of the TOV equations (black solid lines). Colored regions indicate observational constraints that are discussed in the text.

mass configuration is indicated by a green cross<sup>2</sup>. We note that some of the hybrid star sequences (shown by thin black lines) have maximum masses exceeding the value for the

<sup>2</sup> We like to draw the attention of the reader to the appearance of Moiré-like structures in the set of lines in the  $M(R)$  diagram of Fig. 4 that resemble sequences of hybrid stars generated by an equidistant variation of the quark matter EOS parameters  $\eta_D$  and  $\eta_S$ . These structures originate from crossings of the  $M(R)$  lines which collimate in so-called special points [61,62] that are lined up along "trains" [52,63].

purely hadronic neutron star case. This effect apparently contradicts the naive expectation that in the case of a first-order phase transition the maximum mass should generally be lowered, due to the related softening of the EOS. While this effect is observed here too, it may get reversed when the quark matter EOS at high densities becomes stiffer than the hadronic one.

For a comparison we show in Fig. 4 also the regions of mass and radius measurements that will be used to constrain the EOS within the Bayesian analysis performed in this work. The set of data selected for the present study is similar to the choice made by Brandes et al. [9]. It consists of a basic set of observational constraints and additional ones that may have a disputed status or it may be interesting to study the effect of their inclusion on the results of the Bayesian analysis. The basic set contains the precise mass measurement of the high-mass pulsar PSR J0348+0432 in the binary with a white dwarf. It provides a lower limit for the maximum mass:

$$(I) \quad M = 2.10^{+0.04}_{-0.04} M_{\odot} \text{ for PSR J0348+0432 by Antoniadis et al. [64],}$$

In addition, these simultaneous mass-radius measurements of the NICER collaboration belong to the basic set:

$$(II) \quad M = 1.44^{+0.07}_{-0.07} M_{\odot} \text{ and } R = 13.7^{+2.6}_{-1.5} \text{ km for PSR J0030+0451 by Miller et al. [65],}$$

$$(III) \quad M = 2.08^{+0.07}_{-0.07} M_{\odot} \text{ and } R = 13.7^{+2.6}_{-1.5} \text{ km for PSR J0740+6620 by Miller et al. [66], and}$$

$$(IV) \quad M = 1.418^{+0.037}_{-0.037} M_{\odot} \text{ and } R = 11.36^{+0.95}_{-0.63} \text{ km for PSR J0437-4715 by Choudhury et al. [67].}$$

These measurements (I) - (IV) form the basic data set for the present Bayesian inference. The tidal deformability constraint from the binary neutron star merger GW170817 is also an important element of the Bayesian analysis

$$(V) \quad \Lambda_{1.4} = 290^{+290}_{-120} \text{ for GW170817 by Abbott et al. [57].}$$

However, since we want to study the effect of its inclusion on the results of the Bayesian analysis, we display it separately.

Additionally, there are two extreme results that belong to an extended data set:

$$(VI) \quad M = 2.35^{+0.17}_{-0.17} M_{\odot} \text{ for the "black widow" (BW) pulsar PSR J0952-0607 by Romani et al. [68], and}$$

$$(VII) \quad M = 0.77^{+0.20}_{-0.17} M_{\odot} \text{ and } R = 10.04^{+0.86}_{-0.78} \text{ km for HESS J1731-347 by Doroshenko et al. [10] for which we use the shorthand notation "HESS".}$$

The additional constraints that were derived from observations of the binary neutron star merger GW170817 by Bauswein et al. [69] and by Annala et al. [70] provide exclusion regions shown by red rectangular bars in the M-R diagram. They are, however, not taken into account into the Bayesian analysis of the present work. The NICER mass-radius determinations for PSR J0740+6620 by Riley et al. [71] and for PSR J0030+0451 by Raaijmakers et al. [72] as well as the mass measurement for PSR J0740+6620 by Fonseca et al. [73] which updated the earlier one by Cromartie et al. [74] are also not considered in the present Bayesian analysis.

In Fig. 5 we show the tidal deformability as a function of the neutron star mass for the hadronic DD2 reference EOS (green solid line) and the hybrid star sequences (grey lines) of the present study. The data point with error bars corresponds to the gravitational wave analysis of the LIGO Virgo Collaboration for the inspiral phase of the binary neutron star merger GW170817 [57]. The comparison indicates that hybrid star sequences with an early onset of quark deconfinement at masses well below  $1.4 M_{\odot}$  lead to a softening of the EOS at the onset energy density which entails a reduction of the value of the tidal deformability at that mass and thus leads to a fulfillment of the tidal deformability constraint while the DD2 EOS was slightly too stiff to match that constraint.

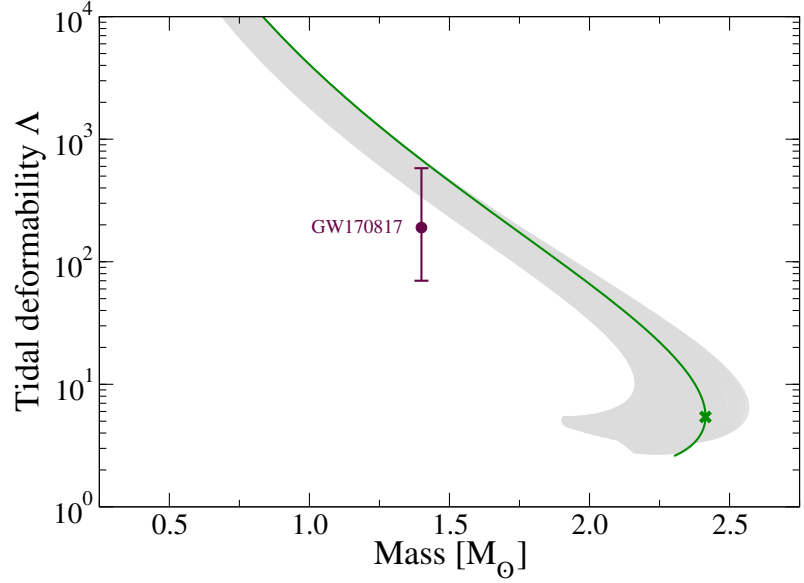


**Figure 5.** Tidal deformability vs. mass for the set of hybrid EoS introduced in this work. The green line highlights the result for the hadronic DD2 EOS and the green cross indicates the maximum mass configuration of that sequence. The data point with error bars corresponds to the gravitational wave analysis of the LIGO Virgo Collaboration for the inspiral phase of the binary neutron star merger GW170817 [57].

#### 4. Bayesian analysis and results for constraining the EOS

Let us describe the Bayesian framework used to infer the posterior distribution of the parameters  $(\eta_D, \eta_V)$  defining EoS, given observational data  $\mathcal{D}$ . Bayes' theorem provides the posterior distribution of the parameters  $(\eta_D, \eta_V)$ ,

$$p((\eta_D, \eta_V)|\mathcal{D}) = \frac{p(\mathcal{D}|\eta_D, \eta_V) p(\eta_D, \eta_V)}{p(\mathcal{D})}, \quad (10)$$

where  $p((\eta_D, \eta_V)|\mathcal{D})$  is the posterior distribution,  $p(\mathcal{D}|\eta_D, \eta_V)$  is the full likelihood,  $p(\eta_D, \eta_V)$  is the prior distribution,  $p(\mathcal{D})$  is the evidence. The prior distribution is taken to be equiprobable

$$p(\eta_D, \eta_V) = \frac{1}{|(\eta_D, \eta_V)|} = \frac{1}{N}. \quad (11)$$

The full likelihood is obtained by production of the likelihoods for all independent observations  $D_\alpha$

$$p(\mathcal{D}|\eta_D, \eta_V) = \prod_{\alpha}^N p(D_\alpha|\eta_D, \eta_V). \quad (12)$$

The likelihood associated with the lower limit of the maximum mass is modeled using a normal cumulative distribution function  $F_N$ ,

$$p(D_{M_{\max}^{(i)}}|\eta_D, \eta_V) = F_N(M_{\max}(\eta_D, \eta_V); \mu_M^{(i)}, \sigma_M^{(i)}), \quad (13)$$

where  $\mu_M^{(i)}$  and  $\sigma_M^{(i)}$  are the mean and standard deviation of the constraint are taken from [64] and [68].

The likelihood for mass-radius constraints is computed via integration over the central density  $\varepsilon_c$  with the appropriate probability density function

$$p(D_{MR^{(i)}}|\eta_D, \eta_V) = \int_{\varepsilon_c^{\min}}^{\varepsilon_c^{\max}(\eta_D, \eta_V)} f_{MR}^{(i)}(M(\varepsilon_c; \eta_D, \eta_V), R(M)) pr(\eta_D, \eta_V) d\varepsilon_c. \quad (14)$$



The probability density functions  $f_{MR}^{(i)}$  have been constructed using Kernel Density Estimation (KDE) [75] based on data obtained from the Zenodo repository for MR constraints: PSR J0030+0451 [76], PSR J0740+6620 [77], and PSR J0437–4715 [78], and HESS J1731–347 [79]. For gravitational wave (GW) data, the likelihood is expressed similarly as an integral over  $\varepsilon_c$

$$p(D_{GW} | (\eta_D, \eta_V)) = \int_{\varepsilon_c^{\min}}^{\varepsilon_c^{\max}(\eta_D, \eta_V)} f_{GW}(\Lambda_1(\varepsilon_c; \eta_D, \eta_V), \Lambda_2(\Lambda_1)) pr(\eta_D, \eta_V) d\varepsilon_c. \quad (15)$$

Here,  $f_{GW}$  is built using the data for GW170817 available from [56]. The evidence  $p(\mathcal{D})$  is obtained by marginalizing over all possible values of  $(\eta_D, \eta_V)$ :

$$p(\mathcal{D}) = \sum_{(\eta_D, \eta_V)} p(\mathcal{D} | (\eta_D, \eta_V)) p(\eta_D, \eta_V). \quad (16)$$

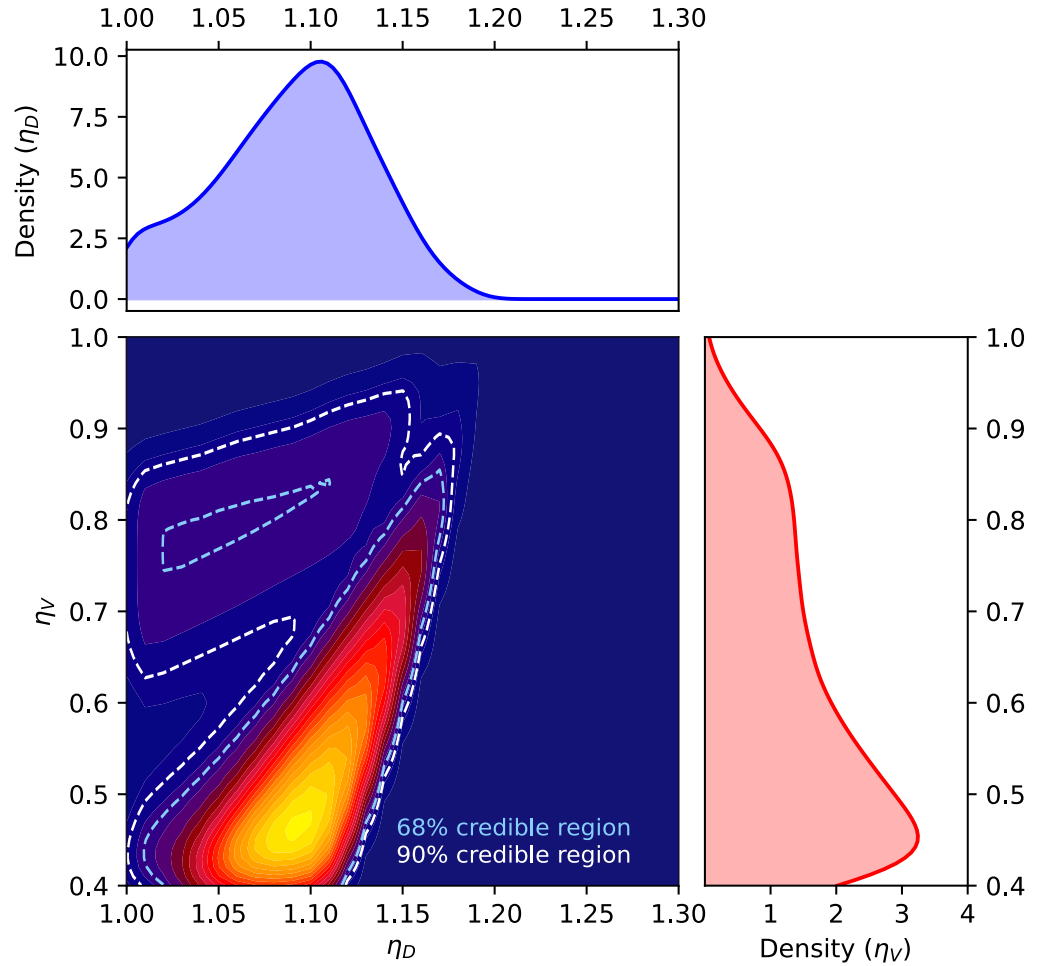


**Figure 6.** Bayesian analysis of the most likely parameter values in the  $\eta_V - \eta_D$  plane under modern observational constraints for masses, radii and the tidal deformability of neutron stars.

The result of the Bayesian analysis is shown in Fig. 6. We observe that the 60% credible region forms a triangular shaped area closely resembling the nearly cigar-shaped region reported in previous works (e.g., in Refs. [16], [40] and [41]), although those results were not derived using a Bayesian analysis. The most favorable parameter set can be read off the peak positions for the marginalized probability distributions in the  $\eta_V$ - and  $\eta_D$ - directions, respectively. These peak positions are very close to the best choice values  $\eta_V = 0.5$  and

$\eta_D = 1.1$  that were found heuristically in [33], where the present class of hybrid EOS was introduced.

In Fig. 7 we show the different cases of phase transitions, with the following color coding:

- White: No Maxwell transition,
- Gray: Maxwell transition occurs after the DD2 instability value (no stable hybrid stars),
- Orange: Maxwell transition starts before the DD2 instability value, with a jump to the DD2 instability (no stable hybrid stars),
- Green: Maxwell transition ends before the DD2 instability value (stable hybrid stars exist)
- Blue: Maxwell transition ends before the DD2 instability value and satisfies the Seidov criterion [80] (extremely light twin stars).

Overlaid to this classification are the credible regions of the Bayesian analysis at the 60% (blue dashed lines) and at the 90% (red dashed lines) confidence level. One can read off from this figure not only the favorable parameter region and deduce the corresponding set of hybrid EOS, but also whether a hybrid star sequence with a color superconducting quark core or even a mass twin solution is favorable.

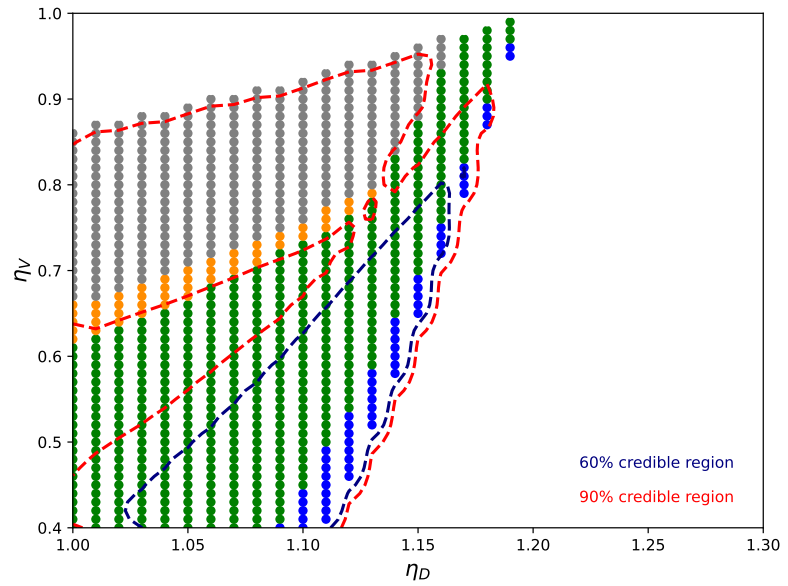


**Figure 7.** Phase transition categories in the  $\eta_V - \eta_D$  diagram, overlaid with the 60% (blue dashed line) and 90% (red dashed lines) credible regions of the Bayesian analysis. For details, see text.

In Fig. 8 we show results of investigating the role that the choice of certain sets of observables has for the topology of favorable regions in the parameter plane as a result of the BA. On eight panels (a) - (h) we show the 60% and 90% confidence regions overlaid to the four types of hybrid star sequences. Starting from panel (a) with the basic set of constraints that excludes the tidal deformability measurement of GW170817, we see two separate regions encircled with the blue dashed lines for the 60% credibility. One lies entirely inside the grey domain which belongs to purely hadronic configurations where no stable hybrid stars exist, the other one is entirely in the green domain corresponding to standard hybrid stars with not too early onset of deconfinement ( $\eta_D \lesssim 1.1$ ) and no twin stars. Since the stiff DD2 hadronic baseline EOS with a maximum mass of  $M = 2.414 M_\odot$  (case A in Tab. 2 reaches well beyond the high-mass constraints (I) and (III), the hybrid

star sequences safely fulfill these constraints with not too large vector meson couplings ( $\eta_V \lesssim 0.6$ ).

When the lower limit on the maximum mass is increased to by adding the black widow pulsar constraint (VI) to the basic set, then the 60% credibility region at large  $\eta_V$  is enlarged and comprises all purely hadronic stars as well as hybrid stars with not too early onset of deconfinement ( $\eta_D \lesssim \eta_{D,\max} - 0.05$  for any  $\eta_V$ ) see panel (h).

When we add constraints to the basic set which require compactness at low mass (GW170817 and/or HESS), we observe that the probability for the purely hadronic EOS is suppressed and the second 60% region in the grey domain is absent on panels (c), (e) and (g). This holds also for the full set of constraints shown on panel (b).

Adding the tidal deformability constraint (V) from GW170817 to the basic set requires the onset masses to be lowered and therefore this drags the high- $\eta_D$  border of the 60% credibility region at lower- $\eta_V$  to maximally admissible  $\eta_D$  values, where even mass twin sequences are possible, see panel (e). This shape is only stretched towards the corner of highest couplings in the parameter plane when additionally the BW constraint (VI) is included, see panel (f). Since panel (f) is very similar to panel (b) for the full set of constraints, one can conclude that out of all additional constraints (V) - (VII), the latter is dominated by the tidal deformability constraint.

In Figs. 9 and 10, we display observables in the plane of the EOS parameters  $\eta_V$  and  $\eta_D$  as color-bubble diagrams overlaid to the Bayesian likelihood contours for the 60% and 90% credibility regions. In Figs. 9 we show the difference in maximum mass between hybrid stars and the DD2 hadronic reference EOS with a maximum mass of  $2.4 M_\odot$  (the black solid neutrality line). The yellow bubble region indicates that no stable hybrid stars are possible there.

We want to mention that in [16], the maximum possible mass was at  $2.35 M_\odot$  and in [40,41] at  $2.42 M_\odot$ . Thus the corresponding parameter sets of the latter works would lie in the corner of the green region, between the 60% and 90% confidence regions, while the present class of hybrid EOS has the parameter sets with the largest maximum masses at the very corner of the green region, outside even the 90% confidence region.

The reason for this region of highest-mass hybrid EOS to be disfavored lies in the fact that they predict hybrid star sequences that are not sufficiently compact in the mass region of  $1.4 M_\odot$ , where the tidal deformability was measured for the binary neutron star merger GW170817 and requires radii in the range  $R_{1.4} = 10.94 - 12.61$  km at 90% confidence [81]. In Figs. 10 we show the tidal deformability constraint:  $70 < \Lambda_{1.4} < 580$  and can observe that the 60% credible region (blue dashed line) encloses the pairs of quark matter parameter values for which the tidal deformability constraint is fulfilled.

In Fig. 11 we show the squared speed of sound as a function of the energy density for the hadronic DD2 reference EOS (green solid line) and the hybrid star EOS with a Maxwell-constructed first-order phase transition to color superconducting 3DFF quark matter fitted to  $c_s^2 = \text{const}$  with a color code of the lines representing the probability after Bayesian analysis as shown in the legend. In the first-order phase transition region holds  $c_s^2 = 0$ . The maximum energy density that can be reached in the center of a neutron star made of DD2 matter for its maximum mass configuration is  $\epsilon_c^{\max} = 1108 \text{ MeV/fm}^3$  (vertical green dashed line, case A) and reduces to  $\epsilon_c^{\max} = 998.5 \text{ MeV/fm}^3$  (vertical blue dotted line, case B) when a deconfinement transition is possible but does not lead to stable hybrid stars. The central energy density of the maximum mass configuration for the hybrid EOS with the highest posterior probability (light blue dashed line, case C) is  $\epsilon_c^{\max} = 1175 \text{ MeV/fm}^3$  while that of the hybrid EOS with highest maximum mass (magenta dashed line, case D) is  $\epsilon_c^{\max} = 931 \text{ MeV/fm}^3$ .

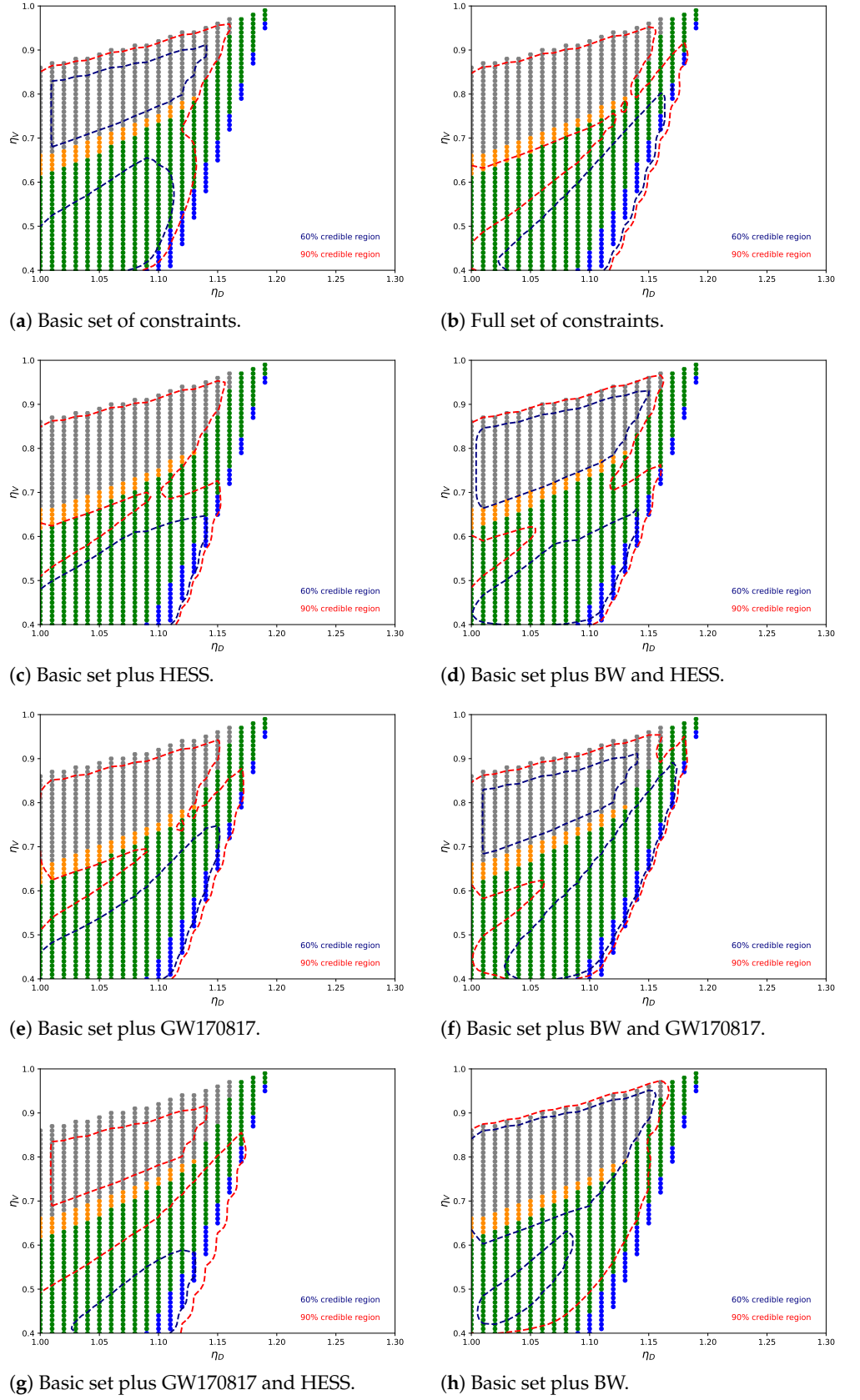


**Figure 8.** Same as Fig. 7 for different sets of constraints. The constraints (I), (II), (III), and (IV) constitute the basic set shown in panel (a), while the full set is shown in panel (b), identical to Fig. 7. Additional constraints (V), (VI), and (VII) are denoted as GW170817, BW, and HESS, respectively, and analysed in different combinations with the basic set in panels (c) - (h).

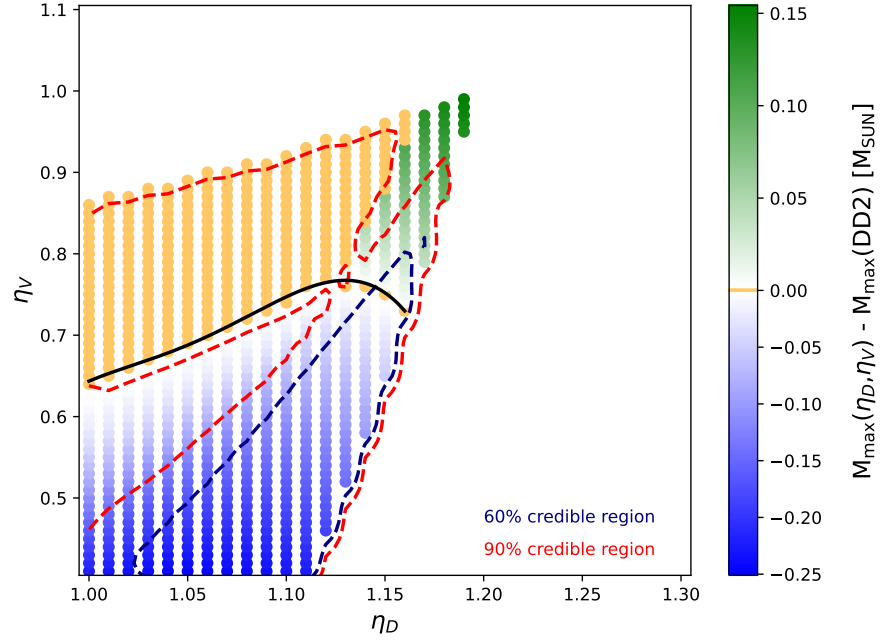


**Figure 9.** Color-bubble diagram for the difference in maximum mass between hybrid stars and the DD2 hadronic reference EOS with a maximum mass of  $2.4 M_{\odot}$  (the black solid neutrality line) in the  $\eta_V$ - $\eta_D$  plane of EOS parameters overlaid to the Bayesian likelihood contours for the 60% and 90% credibility regions.

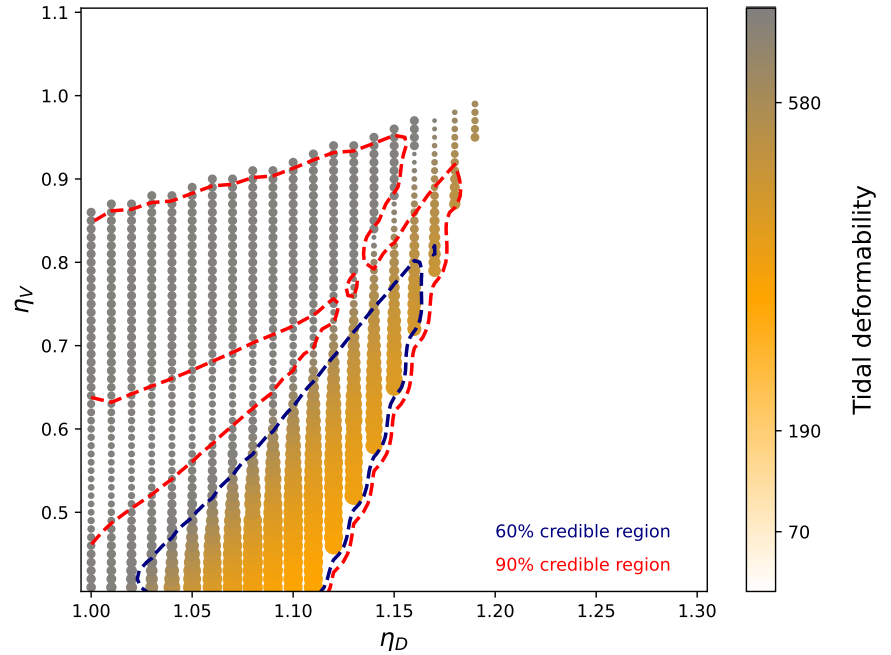


**Figure 10.** Color-bubble diagram for the tidal deformability in the  $\eta_V$ - $\eta_D$  plane of EOS parameters overlaid to the Bayesian likelihood contours for the 60% and 90% credibility regions. On the color legend bar the constraint (V) from the LVC measurement of the tidal deformability for GW170817 is indicated:  $70 < \Lambda_{1.4} < 580$ .

The final result of this Bayesian analysis study for the class of hybrid EOS with the hadronic DD2 RDF reference EOS and the nonlocal 3DFF color superconducting quark matter EOS fitted to the CSS form of EOS is shown in Fig. 12. We note that the EOS parametrisations favored by the Bayesian analysis with the displayed set of observational constraints listed in section 4 provide evidence for an early onset of deconfinement below



|   | $(\eta_D, \eta_V)$<br>– | $M_{\max}$<br>$M_{\odot}$ | $R_{\max}$<br>km | $\varepsilon_{c,\max}$<br>$\text{MeV}/\text{fm}^3$ | $\mu_{c,\max}$<br>MeV | $M_{\text{onset}}$<br>$M_{\odot}$ | $R_{\text{onset}}$<br>km | $\varepsilon_{c,\text{onset}}$<br>$\text{MeV}/\text{fm}^3$ | $\mu_{c,\text{onset}}$<br>MeV |
|---|-------------------------|---------------------------|------------------|--|-----------------------|-----------------------------------|--------------------------|--|-------------------------------|
| A | DD2                     | 2.414                     | 11.84            | 1107.88  | 1909.04               | –                                 | –                        | –  | –                             |
| B | (1.12, 0.76)            | 2.411                     | 12.01            | 1116.29  | 1820.92               | 2.410                             | 12.03                    | 998.54   | 1810.84                       |
| C | (1.08, 0.44)            | 2.195                     | 11.42            | 1175.19  | 1709.54               | 0.630                             | 12.92                    | 234.47   | 1017.95                       |
| D | (1.19, 0.99)            | 2.568                     | 12.54            | 931.18   | 1776.96               | 0.323                             | 13.84                    | 188.38   | 983.82                        |
| E | (1.18, 0.91)            | 2.521                     | 12.38            | 956.42   | 1767.16               | 0.330                             | 13.78                    | 196.10   | 984.87                        |

**Table 2.** Neutron star properties for different special hybrid EoS cases: A – purely hadronic DD2; B – highest onset energy density with a stable hybrid star branch; C – highest posterior probability; D – highest maximum mass; E – highest maximum mass in the 60% credibility area. For details, see text.

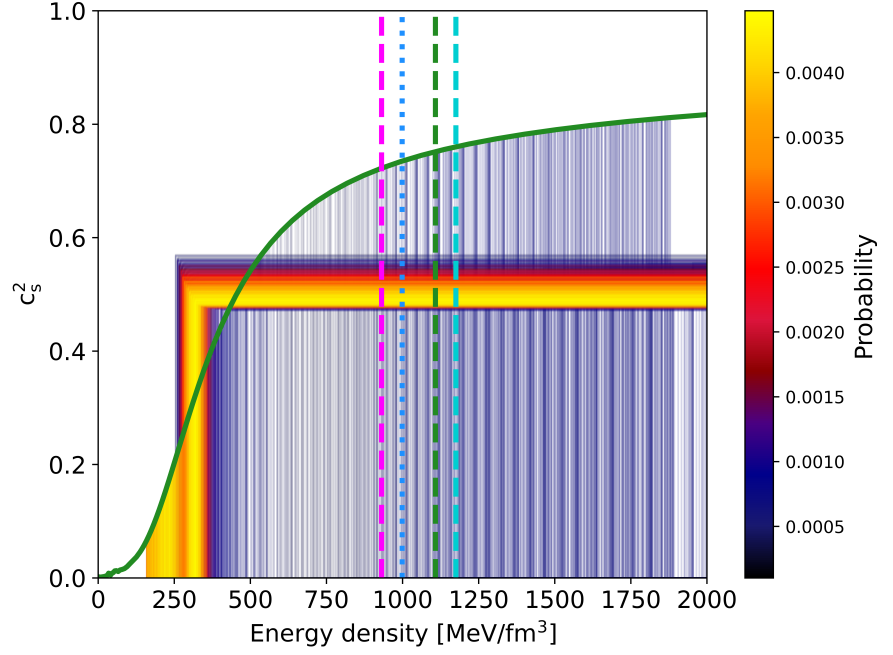


**Figure 11.** Squared speed of sound as a function of the energy density for the hadronic DD2 reference EOS (green solid line), the hybrid star EOS with color superconducting 3DFF quark matter fitted to  $c_s^2 = \text{const}$  (colored lines) with the color code shown in the legend corresponding to the posterior probability after Bayesian analysis. In the first-order phase transition region holds  $c_s^2 = 0$ . The onset (end) of the deconfinement phase transition is marked by vertical lines connecting the bottom of the graph at  $c_s^2 = 0$  with the green DD2 line (the horizontal  $c_s^2 = \text{const}$  lines). The bold vertical lines indicate the central energy densities of the maximum mass configurations for case A: the purely hadronic EOS (green dashed line), case C: the hybrid EOS with the highest posterior probability (blue dashed line) and case D: the hybrid EOS with the highest maximum mass (magenta dashed line) as well as of the onset mass configurations for case B: the hybrid EOS with the highest onset density (blue dotted line).

$0.7 M_{\odot}$  and maximum masses not exceeding  $2.25 M_{\odot}$ . In the region of observed pulsar masses,  $M \sim 1.1 - 2.1 M_{\odot}$ , the radii are approximately mass independent in the range of  $R \sim 12$  km. This feature has been discussed in Ref. [82] as an indicator for maximum masses in the range  $M_{\max} \sim 2.3 - 2.4 M_{\odot}$  within a model-independent study. This is consistent with our result shown in Fig. 12.

## 5. Conclusions

In this work, we have performed for the first time a physics-informed Bayesian analysis of the EOS constraints from modern observational data for masses, radii and the tidal deformability of pulsars within the class of hybrid EOS with a stiff nuclear matter

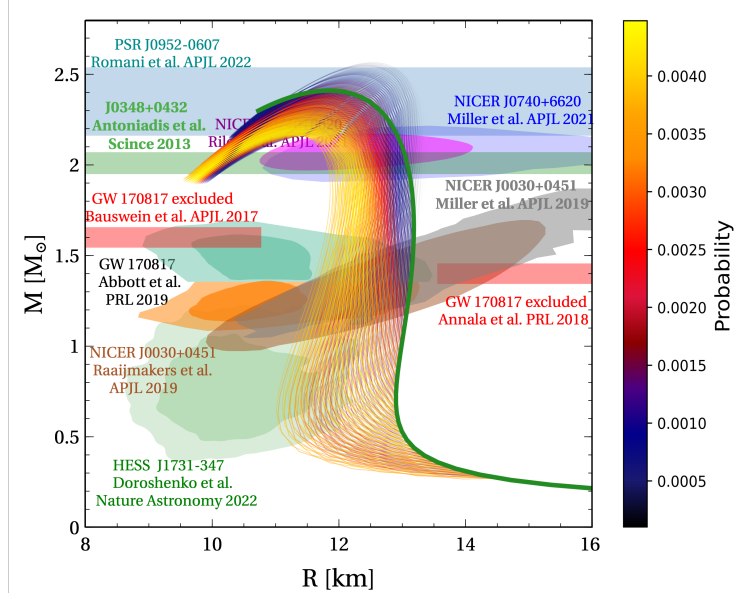


**Figure 12.** Mass-radius diagram showing the hadronic DD2 reference EOS (green solid line) and the hybrid star sequences corresponding to the hybrid EOS Maxwell-constructed from it with the CSS fitted form of the nonlocal 3DFF color superconducting quark matter EOS ((colored lines) with the color code shown in the legend corresponding to the posterior probability after Bayesian analysis with the modern mass-radius constraints (colored and labelled regions).

phase, color superconducting (two-flavor) quark matter and a Maxwell construction for the phase transition. The color superconducting phase of quark matter along with repulsive vector meson interactions is essential for ensuring that the hybrid compact star model matches observational constraints because it allows a sufficiently low threshold density for the onset of deconfinement and a maximum mass of at least  $2 M_{\odot}$ . This scheme supersedes an earlier physics-informed Bayesian analysis study [11] that was performed within the alternative scheme that uses a soft nuclear matter EOS together with a two-zone interpolation scheme for the transition to color superconducting quark matter. While the latter scheme provided hybrid EOS models in the entire rectangular-shaped section of the two-dimensional EOS parameter space spanned by the vector-meson ( $\eta_V$ ) and diquark ( $\eta_D$ ) couplings, the impossibility to perform a Maxwell construction in the former scheme removed the two corners at high- $\eta_V$ -low- $\eta_D$  and high- $\eta_D$ -low- $\eta_V$  in the present work.

Inside the remaining region highlighted by colored dots in Fig. 7, where the Maxwell construction of a phase transition is possible, the following generic structures can be delineated in the  $\eta_V - \eta_D$  plane and are highlighted on Fig. 7 by dots in different colors:

- the rightmost line of proportionality  $\eta_V \propto \eta_D$  with the early onset of deconfinement, eventually accompanied with the mass twin phenomenon (blue dots),
- the region of stable hybrid stars (green dots),
- the upper right corner of this region, where the hybrid stars with highest maximum mass are found which are eventually disfavored because of missing compactness. In the present work, this corner is at  $\eta_V = 0.99$ ,  $\eta_D = 1.19$ , corresponding to  $M_{\max} = 2.57 M_{\odot}$  at  $R_{\max} = 12.4$  km.
- the region parameter region, where the onset of deconfinement is before the maximum central energy density of purely hadronic neutron stars,  $\varepsilon_{c, \text{onset}} < \varepsilon_{c, \text{max}}$  (orange dots), where there are no stable hybrid stars but due to the presence of a deconfinement transition in the EOS the maximum mass is lowered relative to the purely hadronic case,

- the region, where the onset of deconfinement occurs after the maximum central energy density of purely hadronic neutron stars,  $\varepsilon_{c, \text{onset}} > \varepsilon_{c, \text{max}}$  (grey dots).

The main result of the present Bayesian analysis are constrained regions of 60% and 90% credibility in the  $\eta_V - \eta_D$  plane which allow to further constrain the triangular-shaped region that was found earlier in heuristic studies without employing Bayesian analysis methods [14,16,40,41]. We found that EOS in the upper right corner of that triangle which correspond to hybrid stars with maximum masses above the purely hadronic maximum mass of  $2.41 M_\odot$  are incompatible with the 60% credibility region of the Bayesian analysis! This appears to be a consequence of the tidal deformability constraint that disfavors these high-maximum mass hybrid star sequences because of their insufficient compactness. We demonstrated how the choice of a set of mass-radius constraints influences the shape of the credibility regions in the plane of EOS parameters. Small neutron star radii at or below typical binary radio pulsar masses (e.g.,  $R_{1.4} \lesssim 12$  km) as for HESS and GW170817 require an early onset of deconfinement as induced by large values of  $\eta_D \gtrsim 1.1$  (color superconductivity) while the vector coupling responsible for the stiffness of the EOS and large maximum masses can stay at moderate values of  $\eta_V \lesssim 0.5$ . Including the back widow pulsar PSR J0952-0607 into the set of constraints would require EOS with a maximum mass of at least  $2.18 M_\odot$  (the  $1\sigma$  level). In such a case, the Bayesian analysis results in strong vector couplings  $\eta_V \gtrsim 0.5$  for hybrid star sequences. We note that for our choice of a stiff hadronic baseline EOS such as DD2, the maximum mass constraint is always fulfilled already without a deconfinement phase transition. This is reflected also in the Bayesian analysis result which exhibits the parameter region with no stable hybrid stars as favorable at 60% confidence level.

The next step in the development of this physics-informed Bayesian analysis method is the implementation of the requirement that the high-density asymptotics of the hybrid EOS family should be compatible with the perturbative QCD benchmark at densities  $n \geq 40 n_0$ , see [83,84]. A promising and straightforward strategy to achieve this goal is the relaxation of the locality assumption for the vector mean field. This has recently been demonstrated by Ivanytskyi [51]. Work in this direction is in preparation.

**Funding:** A.A. and D.B. were supported by NCN under grant No. 2021/43/P/ST2/03319. A.G.G., G.A.C., and J.P.C. would like to acknowledge CONICET, ANPCyT and UNLP (Argentina) for financial support under grants No. PIP 2022-2024 GI - 11220210100150CO, PICT19-00792, PICT22-03-00799 and X960, respectively.

**Acknowledgments:** We thank Dr. Oleksii Ivanytskyi for providing us with the template of present observational mass and radius constraints for pulsars that we used in preparing figures 4 and 12.

## References

1. Sorensen, A.; et al. Dense nuclear matter equation of state from heavy-ion collisions. *Prog. Part. Nucl. Phys.* **2024**, *134*, 104080, [arXiv:nucl-th/2301.13253]. <https://doi.org/10.1016/j.pnpnp.2023.104080>.
2. Blaschke, D.; Schaffner-Bielich, J.; Schulze, H.J., Eds. *Exotic Matter in Neutron Stars*; Vol. 52, *European Physical Journal A*, Springer, 2016.
3. Rezzolla, L.; Pizzochero, P.; Jones, D.I.; Rea, N.; Vidaña, I., Eds. *The Physics and Astrophysics of Neutron Stars*; Vol. 457, *Astrophysics and Space Science Library*, Springer, 2018. <https://doi.org/10.1007/978-3-319-97616-7>.
4. Chanlaridis, S.; Ohse, D.; Antoniadis, J.; Blaschke, D.; Alvarez-Castillo, D.E.; Danchev, V.; Misra, D.; Langer, N. Formation of twin compact stars in low-mass X-ray binaries: Implications on eccentric and isolated millisecond pulsar populations **2024**. [arXiv:astro-ph.HE/2409.04755].
5. Bauswein, A.; Bastian, N.U.F.; Blaschke, D.B.; Chatziioannou, K.; Clark, J.A.; Fischer, T.; Oertel, M. Identifying a first-order phase transition in neutron star mergers through gravitational waves. *Phys. Rev. Lett.* **2019**, *122*, 061102, [arXiv:astro-ph.HE/1809.01116]. <https://doi.org/10.1103/PhysRevLett.122.061102>.

6. Bauswein, A.; Blacker, S.; Vijayan, V.; Stergioulas, N.; Chatziioannou, K.; Clark, J.A.; Bastian, N.U.F.; Blaschke, D.B.; Cierniak, M.; Fischer, T. Equation of state constraints from the threshold binary mass for prompt collapse of neutron star mergers. *Phys. Rev. Lett.* **2020**, *125*, 141103, [arXiv:astro-ph.HE/2004.00846]. <https://doi.org/10.1103/PhysRevLett.125.141103>.
7. Fischer, T.; Bastian, N.U.F.; Wu, M.R.; Baklanov, P.; Sorokina, E.; Blinnikov, S.; Typel, S.; Klähn, T.; Blaschke, D.B. Quark deconfinement as a supernova explosion engine for massive blue supergiant stars. *Nature Astron.* **2018**, *2*, 980–986, [arXiv:astro-ph.HE/1712.08788]. <https://doi.org/10.1038/s41550-018-0583-0>.
8. Bauswein, A.; Blaschke, D.; Fischer, T., Effects of a strong phase transition on supernova explosions, compact stars and their mergers; 2022; [arXiv:nucl-th/2203.17188]. [https://doi.org/10.1142/9789811220944\\_0008](https://doi.org/10.1142/9789811220944_0008).
9. Brandes, L.; Weise, W.; Kaiser, N. Evidence against a strong first-order phase transition in neutron star cores: Impact of new data. *Phys. Rev. D* **2023**, *108*, 094014, [arXiv:nucl-th/2306.06218]. <https://doi.org/10.1103/PhysRevD.108.094014>.
10. Doroshenko, V.; Suleimanov, V.; Pühlhofer, G.; Santangelo, A. A strangely light neutron star within a supernova remnant. *Nat. Astron.* **2022**, *6*, 1444–1451. <https://doi.org/10.1038/s41550-022-01800-1>.
11. Ayriyan, A.; Blaschke, D.; Grunfeld, A.G.; Alvarez-Castillo, D.; Grigorian, H.; Abgaryan, V. Bayesian analysis of multimessenger M-R data with interpolated hybrid EoS. *Eur. Phys. J. A* **2021**, *57*, 318, [arXiv:astro-ph.HE/2102.13485].
12. Klähn, T.; Blaschke, D.; Sandin, F.; Fuchs, C.; Faessler, A.; Grigorian, H.; Ropke, G.; Trümper, J. Modern compact star observations and the quark matter equation of state. *Phys. Lett. B* **2007**, *654*, 170–176, [nucl-th/0609067]. <https://doi.org/10.1016/j.physletb.2007.08.048>.
13. Blaschke, D.; Fredriksson, S.; Grigorian, H.; Oztas, A.M.; Sandin, F. The Phase diagram of three-flavor quark matter under compact star constraints. *Phys. Rev. D* **2005**, *72*, 065020, [hep-ph/0503194]. <https://doi.org/10.1103/PhysRevD.72.065020>.
14. Klähn, T.; Łastowiecki, R.; Blaschke, D.B. Implications of the measurement of pulsars with two solar masses for quark matter in compact stars and heavy-ion collisions: A Nambu–Jona-Lasinio model case study. *Phys. Rev. D* **2013**, *88*, 085001, [arXiv:nucl-th/1307.6996]. <https://doi.org/10.1103/PhysRevD.88.085001>.
15. Fuchs, C. The Relativistic Dirac-Brueckner approach to nuclear matter. *Lect. Notes Phys.* **2004**, *641*, 119–146, [nucl-th/0309003]. [https://doi.org/10.1007/978-3-540-39911-7\\_4](https://doi.org/10.1007/978-3-540-39911-7_4).
16. Baym, G.; Furusawa, S.; Hatsuda, T.; Kojo, T.; Togashi, H. New Neutron Star Equation of State with Quark-Hadron Crossover. *Astrophys. J.* **2019**, *885*, 42, [arXiv:astro-ph.HE/1903.08963]. <https://doi.org/10.3847/1538-4357/ab441e>.
17. Masuda, K.; Hatsuda, T.; Takatsuka, T. Hadron–quark crossover and massive hybrid stars. *PTEP* **2013**, *2013*, 073D01, [arXiv:nucl-th/1212.6803]. <https://doi.org/10.1093/ptep/ptt045>.
18. Baym, G.; Hatsuda, T.; Kojo, T.; Powell, P.D.; Song, Y.; Takatsuka, T. From hadrons to quarks in neutron stars: a review. *Rept. Prog. Phys.* **2018**, *81*, 056902, [arXiv:astro-ph.HE/1707.04966]. <https://doi.org/10.1088/1361-6633/aae14>.
19. Kaltenborn, M.A.R.; Bastian, N.U.F.; Blaschke, D.B. Quark-nuclear hybrid star equation of state with excluded volume effects. *Phys. Rev. D* **2017**, *96*, 056024, [arXiv:astro-ph.HE/1701.04400]. <https://doi.org/10.1103/PhysRevD.96.056024>.
20. Horowitz, C.J.; Moniz, E.J.; Negele, J.W. Hadron structure in a simple model of quark/nuclear matter. *Phys. Rev. D* **1985**, *31*, 1689–1699. <https://doi.org/10.1103/PhysRevD.31.1689>.
21. Ropke, G.; Blaschke, D.; Schulz, H. Pauli Quenching Effects in a Simple String Model of Quark / Nuclear Matter. *Phys. Rev. D* **1986**, *34*, 3499–3513. <https://doi.org/10.1103/PhysRevD.34.3499>.
22. Ivanytskyi, O.; Blaschke, D. Density functional approach to quark matter with confinement and color superconductivity. *Phys. Rev. D* **2022**, *105*, 114042, [arXiv:nucl-th/2204.03611]. <https://doi.org/10.1103/PhysRevD.105.114042>.
23. Ivanytskyi, O.; Blaschke, D. A new class of hybrid EoS with multiple critical endpoints for simulations of supernovae, neutron stars and their mergers. *Eur. Phys. J. A* **2022**, *58*, 152, [arXiv:nucl-th/2205.03455]. <https://doi.org/10.1140/epja/s10050-022-00808-5>.
24. Fowler, G.N.; Raha, S.; Weiner, R.M. Confinement and Phase Transitions. *Z. Phys. C* **1981**, *9*, 271. <https://doi.org/10.1007/BF01410668>.
25. Plumer, M.; Raha, S.; Weiner, R.M. Effect of confinement on the velocity of sound in quark-gluon plasma. *Phys. Lett. B* **1984**, *139*, 198–202. [https://doi.org/10.1016/0370-2693\(84\)91244-9](https://doi.org/10.1016/0370-2693(84)91244-9).
26. Wen, X.J.; Zhong, X.H.; Peng, G.X.; Shen, P.N.; Ning, P.Z. Thermodynamics with density and temperature dependent particle masses and properties of bulk strange quark matter and strangelets. *Phys. Rev. C* **2005**, *72*, 015204, [hep-ph/0506050]. <https://doi.org/10.1103/PhysRevC.72.015204>.
27. Yin, S.y.; Su, R.K. Consistent thermodynamic treatment for a quark-mass density-dependent model. *Phys. Rev. C* **2008**, *77*, 055204, [arXiv:nucl-th/0801.2813]. <https://doi.org/10.1103/PhysRevC.77.055204>.
28. Xia, C.J.; Peng, G.X.; Chen, S.W.; Lu, Z.Y.; Xu, J.F. Thermodynamic consistency, quark mass scaling, and properties of strange matter. *Phys. Rev. D* **2014**, *89*, 105027, [arXiv:hep-ph/1405.3037]. <https://doi.org/10.1103/PhysRevD.89.105027>.
29. Li, A.; Zuo, W.; Peng, G.X. Massive hybrid stars with a first order phase transition. *Phys. Rev. C* **2015**, *91*, 035803, [arXiv:astro-ph.SR/1503.02739]. <https://doi.org/10.1103/PhysRevC.91.035803>.

30. Lugones, G.; Grunfeld, A.G. Cold dense quark matter with phenomenological medium effects: A self-consistent formulation of the quark-mass density-dependent model. *Phys. Rev. D* **2023**, *107*, 043025, [arXiv:nucl-th/2209.03455]. <https://doi.org/10.1103/PhysRevD.107.043025>.
31. Issifu, A.; da Silva, F.M.; Menezes, D.P. Proto-strange quark stars from density-dependent quark mass model. *Eur. Phys. J. C* **2024**, *84*, 463, [arXiv:nucl-th/2311.12511]. <https://doi.org/10.1140/epjc/s10052-024-12828-0>.
32. Alvarez-Castillo, D.E.; Blaschke, D.B.; Grunfeld, A.G.; Pagura, V.P. Third family of compact stars within a nonlocal chiral quark model equation of state. *Phys. Rev. D* **2019**, *99*, 063010, [arXiv:hep-ph/1805.04105]. <https://doi.org/10.1103/PhysRevD.99.063010>.
33. Contrera, G.A.; Blaschke, D.; Carlomagno, J.P.; Grunfeld, A.G.; Liebing, S. Quark-nuclear hybrid equation of state for neutron stars under modern observational constraints. *Phys. Rev. C* **2022**, *105*, 045808, [arXiv:nucl-th/2201.00477]. <https://doi.org/10.1103/PhysRevC.105.045808>.
34. Akmal, A.; Pandharipande, V.R.; Ravenhall, D.G. The Equation of state of nucleon matter and neutron star structure. *Phys. Rev. C* **1998**, *58*, 1804–1828, [nucl-th/9804027]. <https://doi.org/10.1103/PhysRevC.58.1804>.
35. Togashi, H.; Takano, M. Variational study for the equation of state of asymmetric nuclear matter at finite temperatures. *Nucl. Phys. A* **2013**, *902*, 53–73, [arXiv:nucl-th/1302.4261]. <https://doi.org/10.1016/j.nuclphysa.2013.02.014>.
36. Togashi, H.; Hiyama, E.; Yamamoto, Y.; Takano, M. Equation of state for neutron stars with hyperons by the variational method. *Phys. Rev. C* **2016**, *93*, 035808, [arXiv:nucl-th/1602.08106]. <https://doi.org/10.1103/PhysRevC.93.035808>.
37. Togashi, H.; Nakazato, K.; Takehara, Y.; Yamamuro, S.; Suzuki, H.; Takano, M. Nuclear equation of state for core-collapse supernova simulations with realistic nuclear forces. *Nucl. Phys. A* **2017**, *961*, 78–105, [arXiv:nucl-th/1702.05324]. <https://doi.org/10.1016/j.nuclphysa.2017.02.010>.
38. Typel, S.; Ropke, G.; Klähn, T.; Blaschke, D.; Wolter, H.H. Composition and thermodynamics of nuclear matter with light clusters. *Phys. Rev. C* **2010**, *81*, 015803, [arXiv:nucl-th/0908.2344]. <https://doi.org/10.1103/PhysRevC.81.015803>.
39. Carlomagno, J.P.; Contrera, G.A.; Grunfeld, A.G.; Blaschke, D. Thermal twin stars within a hybrid equation of state based on a nonlocal chiral quark model compatible with modern astrophysical observations. *Phys. Rev. D* **2024**, *109*, 043050, [arXiv:nucl-th/2312.01975]. <https://doi.org/10.1103/PhysRevD.109.043050>.
40. Gärtlein, C.; Ivanytskyi, O.; Sagun, V.; Blaschke, D. Hybrid star phenomenology from the properties of the special point. *Phys. Rev. D* **2023**, *108*, 114028, [arXiv:nucl-th/2301.10765]. <https://doi.org/10.1103/PhysRevD.108.114028>.
41. Gärtlein, C.; Sagun, V.; Ivanytskyi, O.; Blaschke, D.; Lopes, I. Fastest spinning millisecond pulsars: indicators for quark matter in neutron stars? **2024**. [arXiv:nucl-th/2412.07758].
42. Baym, G.; Pethick, C.; Sutherland, P. The Ground state of matter at high densities: Equation of state and stellar models. *Astrophys. J.* **1971**, *170*, 299–317. <https://doi.org/10.1086/151216>.
43. Fortin, M.; Providencia, C.; Raduta, A.R.; Gulminelli, F.; Zdunik, J.L.; Haensel, P.; Bejger, M. Neutron star radii and crusts: uncertainties and unified equations of state. *Phys. Rev. C* **2016**, *94*, 035804, [arXiv:astro-ph.SR/1604.01944]. <https://doi.org/10.1103/PhysRevC.94.035804>.
44. Oertel, M.; Hempel, M.; Klähn, T.; Typel, S. Equations of state for supernovae and compact stars. *Rev. Mod. Phys.* **2017**, *89*, 015007, [arXiv:astro-ph.HE/1610.03361]. <https://doi.org/10.1103/RevModPhys.89.015007>.
45. Typel, S. Equations of state for astrophysical simulations from generalized relativistic density functionals. *J. Phys. G* **2018**, *45*, 114001. <https://doi.org/10.1088/1361-6471/aadea5>.
46. Antonopoulou, D.; Bozzo, E.; Ishizuka, C.; Jones, D.I.; Oertel, M.; Providencia, C.; Tolos, L.; Typel, S. CompOSE: a repository for neutron star equations of state and transport properties. *Eur. Phys. J. A* **2022**, *58*, 254. <https://doi.org/10.1140/epja/s10050-022-00908-2>.
47. Typel, S.; et al. CompOSE Reference Manual. *Eur. Phys. J. A* **2022**, *58*, 221, [arXiv:astro-ph.HE/2203.03209]. <https://doi.org/10.1140/epja/s10050-022-00847-y>.
48. Blaschke, D.B.; Gomez Dumm, D.; Grunfeld, A.G.; Klähn, T.; Scoccola, N.N. Hybrid stars within a covariant, nonlocal chiral quark model. *Phys. Rev. C* **2007**, *75*, 065804, [arXiv:nucl-th/0703088]. <https://doi.org/10.1103/PhysRevC.75.065804>.
49. Gomez Dumm, D.; Blaschke, D.B.; Grunfeld, A.G.; Scoccola, N.N. Phase diagram of neutral quark matter in nonlocal chiral quark models. *Phys. Rev. D* **2006**, *73*, 114019, [arXiv:hep-ph/0512218]. <https://doi.org/10.1103/PhysRevD.73.114019>.
50. Burgio, G.; Schrock, M.; Reinhardt, H.; Quandt, M. Running mass, effective energy and confinement: the lattice quark propagator in Coulomb gauge. *Phys. Rev. D* **2012**, *86*, 014506, [arXiv:hep-lat/1204.0716]. <https://doi.org/10.1103/PhysRevD.86.014506>.
51. Ivanytskyi, O. Asymptotically conformal CFL quark matter within a nonlocal chiral quark model **2024**. [arXiv:hep-ph/2409.05859].
52. Shahrabaf, M.; Antić, S.; Ayriyan, A.; Blaschke, D.; Grunfeld, A.G. Constraining free parameters of a color superconducting nonlocal Nambu–Jona-Lasinio model using Bayesian analysis of neutron stars mass and radius measurements. *Phys. Rev. D* **2023**, *107*, 054011, [arXiv:nucl-th/2105.00029]. <https://doi.org/10.1103/PhysRevD.107.054011>.
53. Lindblom, L. Determining the Nuclear Equation of State from Neutron-Star Masses and Radii. *The Astrophysical Journal* **1992**, *398*, 569. <https://doi.org/10.1086/171882>.



54. Tolman, R.C. Static solutions of Einstein's field equations for spheres of fluid. *Phys. Rev.* **1939**, *55*, 364–373. <https://doi.org/10.1103/PhysRev.55.364>.
55. Oppenheimer, J.R.; Volkoff, G.M. On massive neutron cores. *Phys. Rev.* **1939**, *55*, 374–381. <https://doi.org/10.1103/PhysRev.55.374>.
56. at al, B.A. LIGO-P1800115-v12: GW170817: Measurements of Neutron Star Radii and Equation of State — dcc.ligo.org. <https://dcc.ligo.org/LIGO-P1800115/public>, 2018. [Accessed 24-10-2024].
57. Abbott, B.P.; et al. GW170817: Measurements of neutron star radii and equation of state. *Phys. Rev. Lett.* **2018**, *121*, 161101, [arXiv:gr-qc/1805.11581].
58. Hinderer, T. Tidal Love numbers of neutron stars. *Astrophys. J.* **2008**, *677*, 1216–1220, [arXiv:astro-ph/0711.2420]. [Erratum: *Astrophys. J.* 697, 964 (2009)], <https://doi.org/10.1086/533487>.
59. Damour, T.; Nagar, A. Relativistic tidal properties of neutron stars. *Phys. Rev. D* **2009**, *80*, 084035, [arXiv:gr-qc/0906.0096]. <https://doi.org/10.1103/PhysRevD.80.084035>.
60. Hinderer, T.; Lackey, B.D.; Lang, R.N.; Read, J.S. Tidal deformability of neutron stars with realistic equations of state and their gravitational wave signatures in binary inspiral. *Phys. Rev. D* **2010**, *81*, 123016, [arXiv:astro-ph.HE/0911.3535]. <https://doi.org/10.1103/PhysRevD.81.123016>.
61. Yudin, A.V.; Razinkova, T.L.; Nadyozhin, D.K.; Dolgov, A.D. Special point on the mass radius diagram of hybrid stars. *Astron. Lett.* **2014**, *40*, 201, [arXiv:astro-ph.SR/1404.0865]. <https://doi.org/10.1134/S1063773714040069>.
62. Cierniak, M.; Blaschke, D. The special point on the hybrid star mass–radius diagram and its multi-messenger implications. *Eur. Phys. J. ST* **2020**, *229*, 3663–3673, [arXiv:astro-ph.HE/2009.12353]. <https://doi.org/10.1140/epjst/e2020-000235-5>.
63. Blaschke, D.; Ayriyan, A.; Cierniak, M.; Grunfeld, A.G.; Ivanytskyi, O.; Shahrabaf, M. Special point “trains” in the M-R diagram of hybrid stars. *EPJ Web Conf.* **2022**, *274*, 07011, [arXiv:nucl-th/2211.12626]. <https://doi.org/10.1051/epjconf/202227407011>.
64. Antoniadis, J.; Freire, P.C.C.; Wex, N.; Tauris, T.M.; Lynch, R.S.; van Kerkwijk, M.H.; Kramer, M.; Bassa, C.; Dhillon, V.S.; Driebe, T.; et al. A Massive Pulsar in a Compact Relativistic Binary. *Science* **2013**, *340*, 448, [arXiv:astro-ph.HE/1304.6875]. <https://doi.org/10.1126/science.1233232>.
65. Miller, M.C.; Lamb, F.K.; Dittmann, A.J.; Bogdanov, S.; Arzoumanian, Z.; Gendreau, K.C.; Guillot, S.; Harding, A.K.; Ho, W.C.G.; Lattimer, J.M.; et al. PSR J0030+0451 Mass and Radius from NICER Data and Implications for the Properties of Neutron Star Matter. *The Astrophysical Journal Letters* **2019**, *887*, L24. <https://doi.org/10.3847/2041-8213/ab50c5>.
66. Miller, M.C.; Lamb, F.K.; Dittmann, A.J.; Bogdanov, S.; Arzoumanian, Z.; Gendreau, K.C.; Guillot, S.; Ho, W.C.G.; Lattimer, J.M.; Loewenstein, M.; et al. The Radius of PSR J0740+6620 from NICER and XMM-Newton Data. *The Astrophysical Journal Letters* **2021**, *918*, L28. <https://doi.org/10.3847/2041-8213/ac089b>.
67. Choudhury, D.; Salmi, T.; Vinciguerra, S.; Riley, T.E.; Kini, Y.; Watts, A.L.; Dorsman, B.; Bogdanov, S.; Guillot, S.; Ray, P.S.; et al. A NICER View of the Nearest and Brightest Millisecond Pulsar: PSR J0437–4715. *The Astrophysical Journal Letters* **2024**, *971*, L20. <https://doi.org/10.3847/2041-8213/ad5a6f>.
68. Romani, R.W.; Kandel, D.; Filippenko, A.V.; Brink, T.G.; Zheng, W. PSR J0952–0607: The Fastest and Heaviest Known Galactic Neutron Star. *Astrophys. J. Lett.* **2022**, *934*, L17, [arXiv:astro-ph.HE/2207.05124]. <https://doi.org/10.3847/2041-8213/ac8007>.
69. Bauswein, A.; Just, O.; Janka, H.T.; Stergioulas, N. Neutron-star radius constraints from GW170817 and future detections. *Astrophys. J. Lett.* **2017**, *850*, L34, [arXiv:astro-ph.HE/1710.06843]. <https://doi.org/10.3847/2041-8213/aa9994>.
70. Annala, E.; Gorda, T.; Kurkela, A.; Vuorinen, A. Gravitational-wave constraints on the neutron-star-matter Equation of State. *Phys. Rev. Lett.* **2018**, *120*, 172703, [arXiv:astro-ph.HE/1711.02644]. <https://doi.org/10.1103/PhysRevLett.120.172703>.
71. Riley, T.E.; et al. A NICER View of the Massive Pulsar PSR J0740+6620 Informed by Radio Timing and XMM-Newton Spectroscopy. *Astrophys. J. Lett.* **2021**, *918*, L27, [arXiv:astro-ph.HE/2105.06980]. <https://doi.org/10.3847/2041-8213/ac0a81>.
72. Raaijmakers, G.; et al. A NICER view of PSR J0030+0451: Implications for the dense matter equation of state. *Astrophys. J. Lett.* **2019**, *887*, L22, [arXiv:astro-ph.HE/1912.05703]. <https://doi.org/10.3847/2041-8213/ab451a>.
73. Fonseca, E.; et al. Refined Mass and Geometric Measurements of the High-mass PSR J0740+6620. *Astrophys. J. Lett.* **2021**, *915*, L12, [arXiv:astro-ph.HE/2104.00880]. <https://doi.org/10.3847/2041-8213/ac03b8>.
74. Cromartie, H.T.; et al. Relativistic Shapiro delay measurements of an extremely massive millisecond pulsar. *Nature Astron.* **2019**, *4*, 72–76, [arXiv:astro-ph.HE/1904.06759]. <https://doi.org/10.1038/s41550-019-0880-2>.
75. Chacón, J.E.; Duong, T. Multivariate kernel smoothing and its applications; Chapman & Hall/CRC Monographs on Statistics and Applied Probability, Chapman & Hall/CRC: Philadelphia, PA, 2020.
76. Miller, M.C.; Lamb, F.K.; Dittmann, A.J.; Bogdanov, S.; Arzoumanian, Z.; Gendreau, K.C.; Guillot, S.; Harding, A.K.; Ho, W.C.G.; Lattimer, J.M.; et al. NICER PSR J0030+0451 Illinois-Maryland MCMC Samples **2019**. <https://doi.org/10.5281/zenodo.3473466>.
77. Miller, M.; Lamb, F.K.; Dittmann, A.J.; Bogdanov, S.; Arzoumanian, Z.; Gendreau, K.C.; Guillot, S.; Ho, W.C.G.; Lattimer, J.M.; Morsink, S.M.; et al. NICER PSR J0740+6620 Illinois-Maryland MCMC Samples **2021**. <https://doi.org/10.5281/zenodo.4670689>.

78. Choudhury, D.; Salmi, T.; Serena, V.; Riley, T.; Kini, Y.; Watts, A.L.; Dorsman, B.; Bogdanov, S.; Guillot, S.; Ray, P.S.; et al. Reproduction package for: 'A NICER View of the Nearest and Brightest Millisecond Pulsar: PSR J0437–4715' **2024**. <https://doi.org/10.5281/zenodo.13766753>.
79. Doroshenko, V.; Suleimanov, V.F.; Pühlhofer, G.; Santangelo, A. MCMC samples for X-ray spectra fits summarised in the paper "A strangely light neutron star" **2023**. <https://doi.org/10.5281/zenodo.8232233>.
80. Seidov, Z.F. The Stability of a Star with a Phase Change in General Relativity Theory. *Soviet Astronomy* **1971**, *15*, 347.
81. Dietrich, T.; Coughlin, M.W.; Pang, P.T.H.; Bulla, M.; Heinzl, J.; Issa, L.; Tews, I.; Antier, S. Multimessenger constraints on the neutron-star equation of state and the Hubble constant. *Science* **2020**, *370*, 1450–1453, [[arXiv:astro-ph.HE/2002.11355](https://arxiv.org/abs/2002.11355)]. <https://doi.org/10.1126/science.abb4317>.
82. Ferreira, M.; Providência, C. Constraining neutron star matter from the slope of the mass-radius curves. *Phys. Rev. D* **2024**, *110*, 063018, [[arXiv:nucl-th/2406.12582](https://arxiv.org/abs/2406.12582)]. <https://doi.org/10.1103/PhysRevD.110.063018>.
83. Komoltsev, O.; Kurkela, A. How Perturbative QCD Constrains the Equation of State at Neutron-Star Densities. *Phys. Rev. Lett.* **2022**, *128*, 202701, [[arXiv:nucl-th/2111.05350](https://arxiv.org/abs/2111.05350)]. <https://doi.org/10.1103/PhysRevLett.128.202701>.
84. Gorda, T.; Komoltsev, O.; Kurkela, A. Ab-initio QCD Calculations Impact the Inference of the Neutron-star-matter Equation of State. *Astrophys. J.* **2023**, *950*, 107, [[arXiv:nucl-th/2204.11877](https://arxiv.org/abs/2204.11877)]. <https://doi.org/10.3847/1538-4357/acce3a>.

**Disclaimer/Publisher's Note:** The statements, opinions and data contained in all publications are solely those of the individual author(s) and contributor(s) and not of MDPI and/or the editor(s). MDPI and/or the editor(s) disclaim responsibility for any injury to people or property resulting from any ideas, methods, instructions or products referred to in the content.